JACS
JOURNAL OF THE AMERICAN CHEMICAL SOCIETY
Article
pubs.acs.org/JACS

Methane Oxidation over PdO(101) Revealed by First-Principles Kinetic Modeling

Maxime Van den Bossche* and Henrik Grönbeck*

Department of Applied Physics and Competence Centre for Catalysis, Chalmers University of Technology, 412 58 Göteborg, Sweden

Supporting Information

ABSTRACT: The catalytic oxidation of methane to carbon dioxide and water over PdO(101) is investigated with first-principles based microkinetic modeling. Extensive exploration of the reaction landscape allows for determination of preferred pathways at different reaction conditions. The predicted kinetic behavior is in good agreement with a range of experimental findings including reaction orders in methane, water, and oxygen as well as apparent activation energies. The results consolidate the role of the PdO(101) surface in the activity of PdO catalysts and offer starting points for computational design of materials with improved catalytic activity. Moreover, the study demonstrates the predictive power of first-principles based kinetic modeling for oxide surfaces when hybrid functionals are applied in conjugation with kinetic models that go beyond the mean-field approximation.

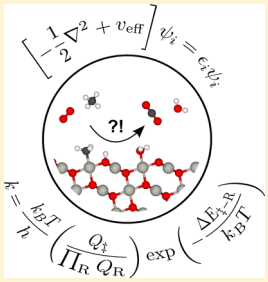

INTRODUCTION

The understanding of complex reaction mechanisms is key in heterogeneous catalysis research as molecular control is mandatory for rational design of superior catalysts.[1] The past decade has witnessed a rapid development of experimental techniques that enable in situ characterization of catalytic reactions.[2,3] Despite these advances, it is generally difficult to follow complete reaction pathways, especially for reactions where competing paths exist and where the dominant mechanism changes with reaction conditions. For such situations, first-principles calculations in combination with microkinetic modeling offer a possibility to explore the reaction kinetics.[4,5] The success of this approach is connected to the ability of the applied electronic structure method (generally density functional theory) to capture the reaction landscape with sufficient accuracy and the microkinetic model to properly describe the adsorbate coverages. Examples where detailed theoretical kinetic models have been used to understand experimentally observed kinetic behavior include NH_3 synthesis over nanoparticle Ru catalysts,[6] CO oxidation over $RuO_2(110)$,[7] ethylene epoxidation over silver catalysts,[8] methanol decomposition over Pt(111),[9] water−gas shift reaction over Cu,[10] and propane dehydrogenation over vanadium oxide.[11]

The catalytic process addressed in this paper is the complex reaction of total oxidation of methane by oxygen, which is a reaction of considerable renewed interest for automotive and sustainable energy applications.[12,13] As methane is a potent greenhouse gas, use of methane as a fuel requires catalysts for abatement of uncombusted emissions.[12] Palladium-based catalysts are considered the most active materials under net oxidizing conditions, whereas platinum generally is used under reducing conditions.[14,15] Ample evidence exists that palladium is present in the form of an oxide when the reaction proceeds in oxygen excess and at temperatures below 950 K.[12,16−19] On the contrary, platinum is not as easily oxidized and oxygen is in this case present in the chemisorbed state.[20]

The PdO(101) facet has over the past years been established as the most active surface of palladium oxide for methane oxidation. The conclusion is based on in situ X-ray diffraction[19] and X-ray photoemission measurements.[21] Furthermore, electronic structure calculations for the dissociative adsorption of methane (commonly assumed to be the rate-limiting step) have shown that the PdO(101) surface provides the lowest energy barrier for this elementary step.[19,21−23] Although PdO(100) is the stable surface orientation of PdO,[24] the initial dissociation barrier is considerably higher on this surface.[19,25,26] Aside from the methane dissociation reaction, the interaction of various reaction intermediates with PdO(101) has previously been investigated, including CO,[27,28] H_2,[29,30] O_2,[31] H_2O,[32] CO_2,[33] and other small alkanes.[22,23,34,35]

Although PdO(101) has been identified as the active PdO termination, fundamental puzzles remain as to the reaction kinetics for the complete conversion of methane to carbon dioxide and water. Little is known, for example, about the reaction pathways beyond the initial dissociation of methane. Such information is needed in order to validate the common assumption that the dissociative adsorption is the rate-limiting step. Knowledge is also absent regarding the elementary reactions that give rise to the Mars−van Krevelen type of mechanism, which has been suggested on the basis of kinetic isotope studies.[36] Additionally, there is as of yet no comprehensive molecular understanding of how the rate of methane conversion is affected by the reaction conditions, i.e., the origins of measured reaction orders and apparent activation energies. Depending on reaction conditions, experimental studies on unsupported PdO catalysts report reaction orders

Received: June 11, 2015
Published: September 2, 2015

DOI: 10.1021/jacs.5b06069
J. Am. Chem. Soc. 2015, 137, 12035−12044

of (i) 0.6−0.7 in methane pressure,[16,37] (ii) close to 0 in oxygen pressure, and (iii) from −1 to 0 in water pressure.[16,37] The measured apparent activation energies vary by as much as 1 eV from 0.3 eV[16] to 1.3 eV.[37] The range of measured apparent activation energies indicates that the reaction path depends on the operational conditions. Previous kinetic models for complete methane oxidation on metal surfaces[20,38,39] have assumed reaction schemes where methane dissociation continues to elemental carbon. This reduction of complexity is clearly an oversimplification for reactions on oxide surfaces where Mars−van Krevelen processes are active.

Here, we apply first-principles microkinetic modeling (FP-MKM) to the nested reaction of complete methane oxidation over PdO(101). An unbiased approach to the reaction scheme allows us to uncover the most probable reaction path which includes early formation of carbon−oxygen bonds where the oxygen in some steps originate from the lattice. The kinetic results are in good agreement with experiments obtained at different reaction conditions. In particular, reaction orders in methane, oxygen and water are reproduced together with the large span of measured apparent activation energies. The good agreement with experiments is possible only if the reaction landscape is described with a hybrid functional and if the MKM is performed beyond the mean-field approximation.

THEORETICAL METHODOLOGY

The applied approach is based on a FP-MKM framework, where a reaction network is constructed using density functional theory (DFT) calculations and where conventional transition state theory is used to describe the reaction kinetics.

Electronic Structure Calculations. For the electronic structure calculations, the plane-wave projector augmented-wave (PAW) code VASP is used,[40−42] with the standard PAW potentials and a kinetic energy cutoff value of 450 eV. All calculations are performed in a (3 × 1) PdO(101) surface unit cell containing four PdO trilayers (48 substrate atoms), as shown in Figure 1. The structures are relaxed

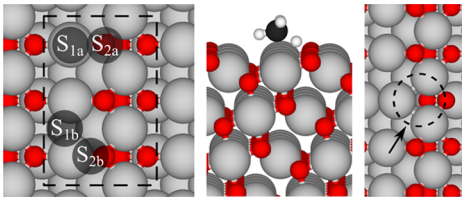

Figure 1. Left: top view of the PdO(101) surface with indication of the employed (3 × 1) surface unit cell and the different types of adsorption sites. Center: tilted view of the transition state for CH_4 dissociation. Right: structural model of a surface oxygen vacancy. Atomic color codes: Pd (gray), O (red), C (black), H (white).

(with the bottom PdO trilayer constrained to bulk positions) until the largest force in the system is smaller than 0.01 eV/Å for the local minima and smaller than 0.05 eV/Å for the transition states.[43,44] The transition states are obtained with the climbing image nudged elastic band[45,46] as well as the dimer method.[47]

The electronic self-interaction error in generalized gradient approximations (GGAs) to the exchange-correlation functional in DFT is known to yield too narrow oxide band gaps. Palladium oxide is one such example, which is predicted to be a zero band gap oxide in GGA, whereas it is measured to have a band gap of about 1 eV.[48,49] The self-interaction error is also manifested in adsorption properties and core-level shifts.[27,50,51] Because of these deficiencies, reaction and activation energies have been evaluated employing the screened hybrid functional HSE06.[52−54] The HSE06 functional does not include van der Waals interactions which may affect some reaction steps. Here, van der Waals contributions evaluated within the Grimme-D3 approach[55] are included for H_2O adsorption (stabilization by 0.19 eV). As we are considering methane oxidation at elevated temperatures, molecularly adsorbed methane is not present on the surface during the reaction, thus, van der Waals corrections are not necessary for adsorbed methane. Spin-polarization is applied in all cases where spin-polarized adsorbates could be envisioned, such as O and O_2. The gas phase radicals are treated in appropriate spin states.

Although the screened HSE06 functional is computationally more efficient than a conventional hybrid functional, the computational cost is still substantial. The HSE06 calculations are, therefore, restricted to single-point energy evaluations, at geometries obtained using the GGA functional proposed by Perdew, Burke, and Ernzerhof (PBE).[56] A comparison of the calculated adsorption energies for O_2, H_2O, CH_3, and H with the adsorption energies obtained with relaxations at the HSE06 level demonstrates that the PBE geometries are sufficient, with maximal differences of 80 meV between both schemes. Normal mode frequencies of the PBE geometries are evaluated in the harmonic approximation using finite differences.

Rate Coefficients. The rate coefficients k for surface reactions between reactants (R) through a transition state (‡) are described via conventional transition state theory,[57,58] using the HSE06 electronic energy barriers and PBE partition functions:

$$k = \frac{k_B T}{h}\left(\frac{Q_{\ddagger}}{\prod_R Q_R}\right)\Bigg|_{PBE} \exp\left(-\frac{\Delta E_{\ddagger-R}}{k_B T}\right)\Bigg|_{HSE06} \quad (1)$$

Here, k_B is the Boltzmann constant, T the temperature, and h Planck's constant. The different translational, rotational, and vibrational partition functions are assumed to be separable ($Q = \prod_i q_i$). The partition functions q_i are calculated with respect to the electronic potential energy minimum and, hence, include contributions from zero-point vibrations. Except for low-barrier rotations, the partition functions for the adsorbed species are described using the quantized harmonic oscillator model. For low-barrier rotations (such as in adsorbed CH_3), the free rotor model was found to be more appropriate. $\Delta E_{\ddagger-R}$ refers to the electronic energy difference between reactant and transition state.

Adsorption events (with activation energy E_a) are treated using kinetic gas theory, where the rate coefficients [in $(s{\cdot}Pa)^{-1}$] are given by

$$k_{ads} = \frac{S_0 A_{site}}{\sqrt{2\pi m_{gas} k_B T}} \exp(-E_a/k_B T) \quad (2)$$

The molecular mass is denoted m_{gas}. The area per adsorption site A_{site} is set to 1 Å^2 and S_0 (prefactor for the sticking coefficient at zero coverage) is assumed to be unity for all gas molecules except methane. For methane adsorption, experimental studies on transition metal surfaces have reported S_0 values in the order of 10^{-4} to 10^{-1} (see ref 59 and references therein). Here we have used a value in the middle of this range, namely 10^{-2}. A value below unity is used to account for the fact that impinging molecules need to approach the active site in a favorable orientation in order to dissociate. Thermodynamic consistency is obeyed for the calculated rate coefficients of adsorption and desorption.

Microkinetic Modeling. The rates r of the individual surface reactions are obtained from the rate coefficients k by multiplying with the coverage of the reactant pairs. Because of the strong attractive adsorbate interactions between several adsorbates (see below), the distribution of the surface species is not well represented within the mean-field approximation, in which it is assumed that the adsorbates are uncorrelated. The concentration of the adsorbate pairs is therefore described in a quasi-chemical formalism, where the relevant adsorbates are subdivided into "paired" and "unpaired" species, which are assumed to be in thermal equilibrium. For example, the coverage of methyl-hydrogen pairs is described by

$$(CH_3)_{unpaired} + (H)_{unpaired} \rightleftharpoons (CH_3 - H)_{paired} \quad (3)$$

DOI: 10.1021/jacs.5b06069
J. Am. Chem. Soc. 2015, 137, 12035−12044

Table 1. Calculated Kinetic Parameters for Reactions Involving Carbonaceous Intermediates[a]

no.	reaction equation	A_{fw}	A_{bw}	$E_{a,fw}^{PBE}$	$E_{a,fw}^{HSE06}$	$E_{a,bw}^{PBE}$	$E_{a,bw}^{HSE06}$
(1)	$CH_4(g) + S_1 - \mathbf{S_2} \rightleftarrows CH_3 - \mathbf{H}$	7.6×10^4	1.8×10^{14}	0.49	0.29	1.08	1.32
(2)	$CH_4(g) + OH + S_1 \rightleftarrows CH_3 + H_2O$	2.8×10^4	1.4×10^{13}	0.35	0.30	0.93	1.08
(3)	$CH_4(g) + OH - \mathbf{H} + S_1 \rightleftarrows CH_3 + H_2O + \mathbf{H}$	"	"	0.36	0.24	0.88	0.62
(4)	$CH_4(g) + OH + S_1 + \mathbf{H} \rightleftarrows CH_3 - \mathbf{H} + H_2O$	"	"	0.39	0.04	1.16	1.32
(5)	$CH_4(g) + OH - \mathbf{H} + S_1 + \mathbf{H} \rightleftarrows CH_3 - \mathbf{H} + H_2O + \mathbf{H}$	"	"	0.68	0.69	1.38	1.62
(6)	$CH_4(g) + O \rightleftarrows CH_3 + OH$	6.7×10^4	7.7×10^{13}	0.57	0.33	2.24	1.77
(7)	$CH_4(g) + O_2 \rightleftarrows CH_3 + OOH$	–	–	1.77	2.26	–	–
(8)	$CH_3 - \mathbf{H} + OH \rightleftarrows CH_2 - \mathbf{H} + H_2O$	3.6×10^{12}	8.3×10^{13}	1.26	1.14	1.14	1.15
(9)	$CH_3 - \mathbf{H} + OH - \mathbf{H} \rightleftarrows CH_2 - \mathbf{H} + H_2O + \mathbf{H}$	"	"	1.60	2.08	1.42	1.03
(10)	$CH_3 - \mathbf{H} + O \rightleftarrows CH_2OH - \mathbf{H} + S_1$	1.1×10^{13}	1.0×10^{15}	0.88	0.73	2.32	2.37
(11)	$CH_3 - \mathbf{H} \rightleftarrows S_1 + CH_3(g) + \mathbf{H}$	1.0×10^{16}	2.6×10^7	2.29	2.74	0.00	0.00
(12)	$CH_3 + OH \rightleftarrows CH_2 + H_2O$	3.6×10^{12}	8.3×10^{13}	1.20	0.83	1.02	1.14
(13)	$CH_3 + OH - \mathbf{H} \rightleftarrows CH_2 + H_2O + \mathbf{H}$	"	"	1.25	1.16	1.12	0.84
(14)	$CH_3 + O \rightleftarrows CH_2OH + S_1$	1.1×10^{13}	1.0×10^{15}	0.93	0.47	2.57	3.31
(15)	$CH_3 + O_2 \rightleftarrows CH_3OO + S_1$	–	–	1.35	1.11	–	–
(16)	$CH_3 + \mathbf{S_2} \rightleftarrows CH_2 - \mathbf{H}$	7.9×10^{12}	1.5×10^{14}	1.49	1.29	1.33	1.71
(17)	$CH_3 + \mathbf{S_2} \rightleftarrows S_1 + \mathbf{CH_3}$	4.6×10^{13}	1.0×10^{15}	1.52	1.15	1.92	2.09
(18)	$CH_3 - \mathbf{Vac} + \mathbf{S_2} \rightleftarrows CH_2 - \mathbf{H} + \mathbf{Vac}$	"	"	1.44	1.44	1.08	1.34
(19)	$CH_3 \rightleftarrows S_1 + CH_3(g)$	1.0×10^{16}	2.6×10^7	2.10	1.54	0.00	0.00
(20)	$\mathbf{CH_3} + O \rightleftarrows \mathbf{CH_2} + OH$	3.9×10^{13}	7.5×10^{13}	0.24	0.19*	2.13	3.30
(21)	$\mathbf{CH_3} + OH \rightleftarrows \mathbf{CH_2} + H_2O$	4.9×10^{13}	4.0×10^{13}	0.78	0.29*	1.50	2.25
(22)	$\mathbf{CH_3} + OH - \mathbf{H} \rightleftarrows \mathbf{CH_2} + H_2O + \mathbf{H}$	"	"	1.05	1.15	1.97	2.38
(23)	$\mathbf{CH_3} \rightleftarrows \mathbf{S_2} + CH_3(g)$	1.9×10^{17}	2.6×10^7	1.94	1.96	0.00	0.00
(24)	$CH_2 - \mathbf{H} + OH \rightleftarrows CH_2OH - \mathbf{H} + S_1$	1.1×10^{13}	8.6×10^{13}	1.29	0.31	1.76	1.29
(25)	$CH_2 - \mathbf{H} + OH - \mathbf{H} \rightleftarrows CH_2OH - \mathbf{H} + \mathbf{H} + S_1$	"	"	1.29	1.11	1.70	1.03
(26)	$CH_2 - \mathbf{H} + \mathbf{S_2} \rightleftarrows \mathbf{CH_2} + \mathbf{H}$	3.7×10^{13}	1.2×10^{14}	1.40	1.29	1.66	2.15
(27)	$CH_2 + OH \rightleftarrows CH_2OH + S_1$	1.1×10^{13}	8.6×10^{13}	0.79	0.06	1.51	1.94
(28)	$CH_2 + OH - \mathbf{H} \rightleftarrows CH_2OH + \mathbf{H} + S_1$	"	"	0.89	0.19	1.55	1.01
(29)	$CH_2 + O_2 \rightleftarrows CH_2OO + S_1$	–	–	1.23	0.79	–	–
(30)	$CH_2 + \mathbf{S_2} \rightleftarrows CH - \mathbf{H}$	1.1×10^{14}	1.3×10^{14}	1.59	1.23	1.04	1.63
(31)	$CH_2 + \mathbf{S_2} \rightleftarrows \mathbf{CH_2} + S_1$	3.7×10^{13}	1.2×10^{14}	1.06	0.22	1.56	1.97
(32)	$\mathbf{CH_2} + S_1 \rightleftarrows CH_2O - \mathbf{Vac}$	5.5×10^{13}	1.2×10^{12}	0.47	0.82	0.34	0.22
(33)	$CH_2OH + \mathbf{S_2} \rightleftarrows CH_2O - \mathbf{H}$	5.4×10^{13}	1.5×10^{12}	0.25	0.21	0.34	0.52
(34)	$CH_2O + \mathbf{S_2} \rightleftarrows CHO - \mathbf{H}$	8.8×10^{12}	2.8×10^{14}	0.48	0.69	1.75	2.19
(35)	$CH_2O + OH \rightleftarrows CHO + H_2O$	1.5×10^{13}	1.0×10^{14}	0.36	0.52	1.62	2.01
(36)	$CH_2O + OH - \mathbf{H} \rightleftarrows CHO + H_2O + \mathbf{H}$	"	"	0.26	0.37	1.45	0.80
(37)	$CH_2O \rightleftarrows S_1 + CH_2O(g)$	4.8×10^{15}	1.8×10^7	0.53	0.55	0.00	0.00
(38)	$CH + \mathbf{S_2} \rightleftarrows C - \mathbf{H}$	3.5×10^{13}	6.0×10^{13}	1.23	1.31	1.21	1.42
(39)	$CH + \mathbf{S_2} \rightleftarrows CHO + \mathbf{Vac}$	6.1×10^{12}	5.3×10^{12}	0.47	0.32	2.15	2.17
(40)	$CHO - \mathbf{H} + OH \rightleftarrows CO + \mathbf{H} + H_2O$	2.1×10^{14}	3.2×10^{13}	0.32	0.33	0.00	0.00
(41)	$CHO + \mathbf{S_2} \rightleftarrows CO + \mathbf{H}$	3.9×10^{14}	2.8×10^{14}	0.77	0.78	1.80	2.44
(42)	$CHO + \mathbf{S_2} \rightleftarrows S_1 + \mathbf{CHO}$	4.5×10^{13}	5.2×10^{13}	0.69	0.71	0.69	1.19
(43)	$CHO + OH \rightleftarrows CO + H_2O$	2.1×10^{14}	3.2×10^{13}	0.49	0.58	1.45	2.88
(44)	$\mathbf{CHO} + S_1 \rightleftarrows CO_2(g) + H + \mathbf{Vac}$	9.2×10^{12}		0.68	1.08		
(45)	$\mathbf{CHO} + OH \rightleftarrows CO(g) + H_2O$	1.8×10^{14}		0.79	0.29*		
(46)	$\mathbf{CHO} + S_1 \rightleftarrows CHOO - \mathbf{Vac}$	1.3×10^{13}	4.3×10^{12}	0.10	0.12	0.62	0.09
(47)	$CHOO - \mathbf{Vac} + \mathbf{S_2} \rightleftarrows CO_2(g) + S_1 + \mathbf{Vac} + \mathbf{H}$	4.4×10^{14}		1.22	1.41		
(48)	$CHOO + \mathbf{S_2} \rightleftarrows CO_2(g) + S_1 + \mathbf{H}$	3.2×10^{14}		1.79	1.83		
(49)	$CHOO + OH \rightleftarrows CO_2(g) + H_2O + S_1$	4.4×10^{14}		1.84	1.95		
(50)	$CO \rightleftarrows S_1 + CO(g)$	7.7×10^{15}	1.9×10^7	1.47	1.40	0.00	0.00
(51)	$CO + \mathbf{S_2} \rightleftarrows S_1 + \mathbf{CO}$	4.7×10^{12}	7.8×10^{12}	0.62	0.45	0.06	0.07
(52)	$\mathbf{CO} + S_1 \rightleftarrows CO_2 - \mathbf{Vac}$	8.1×10^{12}	2.1×10^{12}	0.11	0.41	0.83	0.84
(53)	$CO_2 - \mathbf{Vac} \rightleftarrows S_1 + CO_2(g) + \mathbf{Vac}$	1.9×10^{14}	1.5×10^7	0.38	0.69	0.00	0.00
(54)	$CO + O \rightleftarrows CO_2(g) + 2\ S_1$	2.3×10^{13}		0.49*	0.19*		
(55)	$CO + O_2 \rightleftarrows O + CO_2(g) + S_1$	5.71×10^{12}		1.01	1.51		
(56)	$CO + OH \rightleftarrows HOCO + S_1$	1.1×10^{13}	6.3×10^{13}	0.35	0.32	0.44	0.53
(57)	$HOCO + \mathbf{S_2} \rightleftarrows CO_2(g) + S_1 + \mathbf{H}$	1.5×10^{14}		0.14	0.22		

[a]The values for the pre-exponential factors (s^{-1}) are calculated at 700 K and 1 bar. The electronic energy barriers are in eV. Reactants adsorbed on Pd and O sites are in regular and bold font, respectively. Activation energies denoted with * correspond to the barrier for diffusion of the reactants, as the actual reaction is barrierless.

DOI: 10.1021/jacs.5b06069
J. Am. Chem. Soc. 2015, 137, 12035−12044

Table 2. Calculated Kinetic Parameters for Reactions between O_xH_y Species[a]

no.	reaction equation			A_{fw}	A_{bw}	$E_{a,fw}^{PBE}$	$E_{a,fw}^{HSE06}$	$E_{a,bw}^{PBE}$	$E_{a,bw}^{HSE06}$
(1)	H_2O	⇄	$S_1 + H_2O(g)$	3.6×10^{15}	2.3×10^{7}	1.19	1.38	0.00	0.00
(2)	H_2O–OH	⇄	$OH + S_1 + H_2O(g)$	"	"	1.57	1.73	0.00	0.00
(3)	H_2O–(OH–**H**)	⇄	OH–**H** + $S_1 + H_2O(g)$	"	"	1.63	1.88	0.00	0.00
(4)	H_2O + $\mathbf{S_2}$	⇄	OH–**H**	1.3×10^{13}	6.3×10^{13}	0.22	0.13	0.10	0.23
(5)	H_2O–OH + $\mathbf{S_2}$	⇄	OH–**H** + OH	"	"	0.69	0.59	0.02	0.09
(6)	H_2O–(OH–**H**) + $\mathbf{S_2}$	⇄	2 OH–**H**	"	"	0.62	0.54	0.00	0.04
(7)	$O_2(g) + S_1$	⇄	O_2	1.8×10^{7}	9.9×10^{15}	0.00	0.00	1.25	0.58
(8)	$O_2 + S_1$	⇄	2 O	3.0×10^{13}	2.8×10^{13}	1.61	2.01	1.17	0.42
(9)	$O_2(g)$ + **Vac**	⇄	**O**	1.8×10^{7}	2.2×10^{16}	0.00	0.00	1.41	1.71
(10)	**O** + S_1	⇄	O + $\mathbf{S_2}$	2.7×10^{13}	2.0×10^{13}	0.53	1.16	1.51	1.17
(11)	O + **Vac**	⇄	S_1 + $\mathbf{S_2}$	2.3×10^{13}	6.1×10^{13}	0.49*	0.19*	2.08	2.93
(12)	O_2 + **Vac**	⇄	O + $\mathbf{S_2}$	1.3×10^{16}	1.1×10^{14}	0.80	0.73	1.94	1.87
(13)	OH	⇄	S_1 + OH(g)	2.8×10^{16}	2.4×10^{7}	3.01	2.26	0.00	0.00
(14)	OH–**H**	⇄	S_1 + OH(g) + **H**	"	"	3.06	3.37	0.00	0.00
(15)	$H_2O(g) + O + S_1$	⇄	2 OH	2.3×10^{7}	8.3×10^{15}	0.00	0.00	1.92	1.67
(16)	**H** + S_1	⇄	OH + **Vac**	6.7×10^{13}	1.5×10^{13}	0.68	1.43	0.37	0.29*
(17)	**H** + S_1	⇄	H + $\mathbf{S_2}$	2.3×10^{14}	3.2×10^{13}	1.31	1.93	0.83	0.83
(18)	H–**H**	⇄	H_2 + $\mathbf{S_2}$	1.6×10^{14}	1.3×10^{13}	1.18	1.49	0.38	0.29
(19)	H_2	⇄	$S_1 + H_2(g)$	4.6×10^{14}	7.0×10^{7}	0.49	0.63	0.00	0.00

[a]The values for the pre-exponential factors (s^{-1}) are calculated at 700 K and 1 bar. The electronic energy barriers are in eV. Reactants adsorbed on Pd and O sites are in regular and bold font, respectively. Activation energies denoted with * correspond to the barrier for diffusion of the reactants, as the actual reaction is barrierless.

The attractive interactions are not strictly short-range, e.g., the stability of next-nearest-neighbor CH_3–H adsorbate pairs is in between that of the nearest-neighbor pair and of the unpaired adsorbates. As a compromise between complexity and accuracy, an effective pair formation energy is used, which is the average of the nearest- and next-nearest neighbor pair formation energies. Additionally, the partition functions of the paired species are not calculated explicitly, but are taken equal to the product of the partition functions of the corresponding unpaired species. Thus, the difference in free energy between the paired and unpaired species is given by the difference in electronic energy. These energies are reported below in Figure 3.

In order to obtain the steady-state coverages and reaction rates, the resulting set of coupled differential equations

$$\left(\frac{\partial \theta_i(t)}{\partial t} = \sum_j c_{ij} r_j(\theta_1(t),\ldots,\theta_N(t)) \right)_{i=1,\ldots,N} \quad (4)$$

is integrated numerically using the SciPy Python package, which applies the odepack FORTRAN library.[60] In eq 4, $\theta_i(t)$ is the coverage of adsorbate i at time t, c_{ij} are the stoichiometric numbers, and r_j the elementary reaction rates. Further documentation of the kinetic modeling approach is provided in the Supporting Information.

RESULTS AND DISCUSSION

The results are presented in two parts. First, the reaction network and the calculated kinetic parameters are described. Next, the results from kinetic simulations of the reaction network are presented.

Reaction Database and Kinetic Parameters. One of the objectives with the current study is to establish the preferred reaction path for complete methane oxidation over palladium oxide. In order to do this, a range of possible intermediates and reactions paths are explored (Table 1 and Table 2).

Potential carbonaceous intermediates are situated on under-coordinated Pd sites and/or undercoordinated O sites, see Figure 1). Two sites are associated with the undercoordinated Pd atoms, namely S_{1a} (atop) and S_{1b} (bridge). For the undercoordinated O sites, there is one atop site (S_{2a}) and one O–Pd bridge site (S_{2b}). The preferred adsorption configurations for the considered surface species are S_{1a} for CH_3, CH_2O, CO, and CO_2 whereas it is S_{1b} for CH_2, CH, C, CH_2OH, CHO, HOCO, and HCOO. Species that can form bonds to the undercoordinated O sites are CH_3 (S_{2a}), CH_2 (S_{2b}), CHO (S_{2a}), and CO (S_{2b}).

The identified oxygen–hydrogen compounds are H_2O (S_{1a}), OH (S_{1b}), O_2 (S_{1b}), O (S_{1b}) and H (S_{1a}), which all are adsorbed on the undercoordinated Pd sites. Regarding the oxygen site, atomic H and O adsorb preferably at S_{2a} and S_{2b}, respectively. In addition to the surface species, also a surface oxygen vacancy is considered in the reaction scheme (see Figure 1).

To describe the conversion from methane to carbon dioxide and water, transition states are evaluated for reactions between the carbonaceous intermediates and the different possible oxidizing agents, namely the undercoordinated surface O atoms and the OH, O_2 and O species. The different reactions that have been considered are shown in Table 1.

Methane dissociation is investigated both over the S_{1a} site and by reaction with adsorbed OH, O, and O_2 species (reactions 1–7). The activation energies with respect to gas phase methane are found to be about 0.3 eV with the exception of the reaction with adsorbed O_2 where the barrier is high.[61] The transition state is shown in Figure 2. Methane is close to the S_1 site at the transition state with a Pd–C bond distance of 2.23 Å. Upon dissociation, a methyl group is formed and a hydrogen atom is transferred to the oxidizing agent. Methyl is reacting in a similar fashion with surface species or a lattice oxygen atom (reactions 8–23). A low activation energy (0.47 eV) is predicted for the reaction with adsorbed O forming CH_2OH. The transition state for this reaction is shown in Figure 2. Oxygen is in the transition state located in an atop site and the barrier is related both to this diffusion and the elongation of the C–H bond. After the hydrogen transfer the OH group is bonded to CH_2 in a barrierless fashion. Methyl dissociation to methylene has activation energies that are higher by about 0.4 eV. There is a clear difference (0.3 eV) in

DOI: 10.1021/jacs.5b06069
J. Am. Chem. Soc. 2015, 137, 12035–12044

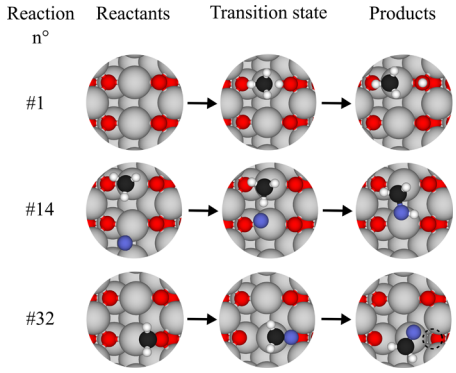

Figure 2. Views of the initial, transition, and final states for three relevant elementary reactions (numbering as in Table 1). Color code as in Figure 1 with adsorbed oxygen colored blue.

activation energies depending on whether the methyl in the initial state is paired with hydrogen or not. The subsequent reactions (24−57) are mainly C−H dissociation reactions and C−O bond formation reactions with eventual formation of CO_2. Notably, we find Mars−van Krevelen reactions to proceed with moderate to low activation energies. One example is reaction (32) where formaldehyde is formed from CH_2 adsorbed on S_{2b} with an activation energy of 0.82 eV. The transition state for this reaction is shown in Figure 2. As CH_2 predominantly is formed on the S_{1b} site, the insertion of oxygen is preceded by S_{1b} to S_{2b} hopping (reaction 31). A second example is CO_2 formation via reactions (51) and (52). Also in this case, CO diffusion toward the S_{2b} occurs prior to the oxygen incorporation. A similar mechanism has previously been discussed in connection with CO oxidation over PdO(101).[28]

Because the adsorbed OH and lattice O turned out to be the important reaction partners for oxidation of CH_x species all possibilities involving adsorbed O_2 or O as oxidants were not considered.

In addition to reactions that consider carbonaceous compounds, investigated reactions that only involve oxygen−hydrogen species are collected in Table 2. H_2O adsorption and dissociation are described by reactions (1−6). Water has a sizable adsorption energy which is further enhanced (~0.3 eV) in the presence of OH-groups. The existence of such hydrogen-bonded complexes on PdO(101) has been investigated previously.[32] Water dissociation is found to be slightly exothermic in the absence of OH-groups, whereas the reaction becomes endothermic upon formation of hydrogen bonds to adsorbed OH.

Reactions (7−12) concern the interaction of atomic and molecular oxygen with the pristine surface and oxygen vacancies. O_2 is preferably adsorbed in a bridge position between two 3-fold coordinated Pd-atoms. O_2 interacts strongly with vacancies and the relaxed structure is the same as for a single O atom adsorbed in the S_{2b}-site. Thus, surface vacancies are easily healed in an oxygen rich atmosphere. Reactions (13−19) in Table 2 describe hydroxyl desorption and disproportionation together with formation of H_2 from adsorbed hydrogen. One of these reactions (16), is the formation of an OH-group at the S_{1b} site and an oxygen vacancy from hydrogen adsorbed on S_{2a}.

The reaction and activation energies are calculated in both PBE and HSE06. There are distinct differences between the two functionals. The barriers for C−H scission are typically lower in the hybrid functional, where methane dissociation is one example which in PBE has a barrier of 0.49 eV, whereas the HSE06 barrier is 0.29 eV. Also the C−O bonds are affected by the choice of functional. One example is the CH_2OH formation from CH_2 and OH adsorbed on S_{1b} sites which is reduced by 0.7 eV going from PBE to HSE06. Yet another striking difference is the adsorption energy of O_2 on the bare surface, which is reduced by 0.7 eV when the hybrid functional is applied. The O_2 adsorption energy calculated within HSE06 is in good agreement with temperature-programmed desorption (TPD) measurements.[62] Water adsorption is affected in the opposite direction, though not to the same degree. These differences have marked effects on the description of the complete oxidation reaction, as PBE will predict surface poisoning by molecular oxygen, whereas HSE06 gives the experimentally observed blocking of water at low temperature.

The calculated reaction landscape reveals interesting effects with respect to coadsorption. Most notable is that several species adsorbed on the undercoordinated Pd sites can be stabilized by the presence of adsorbates on neighboring O sites. Such effects may influence the reaction kinetics in the sense that all adsorbates should not be treated in an uncorrelated manner. The stabilization (in both PBE and HSE06) for a set of surface species (X) owing to H adsorption on S_{2a} is shown in Figure 3. The X−H pair formation energy is calculated as the

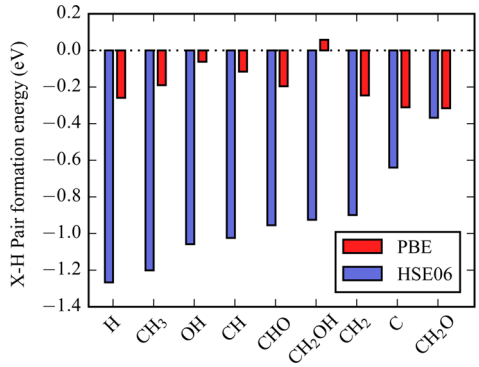

Figure 3. Calculated reaction energies for the formation of adsorbate pairs with the PBE and the HSE06 functionals. The pairing occurs between various adsorbates residing on 3-fold Pd sites and a hydrogen adsorbate on a 3-fold O site.

difference having the adsorbates as nearest neighbors or in two separate surface cells, respectively. The choice of functional has pronounced effects on the pair formation energy and for the most stable pairs, the HSE06 enhances the stabilization by 1 eV with respect to PBE. The dependence on functional can be related to the fact that the hybrid functional correctly captures the semiconducting character of PdO (with a calculated band gap of about 1 eV in the bulk) whereas the PBE functional describes PdO as a semimetal with a finite density of state at the Fermi level.[50]

The bonding of radicals such as CH_3 to Pd sites leads to a depletion of states at the top of the valence band. Adsorption of H to O sites, instead, results in occupation of states in the conduction band (see Supporting Information). Simultaneous adsorption of CH_3 and H results in a recombination between the electronic hole and the electron and a stabilization of the adsorption energy. The magnitude of this effect is not fully captured in the semimetallic (PBE) description of the electronic structure. In addition to the pairs in Figure 3, there exist attractive interactions on the order of 0.3−0.4 eV between

DOI: 10.1021/jacs.5b06069
J. Am. Chem. Soc. 2015, 137, 12035−12044

surface oxygen vacancies and CH_3, CH_2O, and CHOO. For these interactions, both functionals are in fair mutual agreement (within 0.1 eV). The attractive adsorbate−adsorbate interaction owing to electron pairing is different in character as compared to stabilization via hydrogen bonds and has previously been reported for ionic oxides such as MgO and BaO.[63,64]

The stabilization through pair formation affects the ability of the constituents to react with other adsorbates. Generally, the paired species are less reactive than the unpaired counterparts. To account for this, activation barriers have been evaluated for both the paired and unpaired situations. One example is the reaction of CH_3 and atomic oxygen to CH_2OH. The barrier is 0.73 eV when CH_3 is paired with H (reaction 10) whereas it is 0.47 eV in the unpaired case (reaction 14).

Kinetic Simulations. The validity of the presented energy landscape is demonstrated by the ability to reproduce measured kinetic data obtained at a wide range of the reaction conditions where Pd is in a bulk oxidized phase. In order to eliminate possible support effects, we consider experiments performed on unsupported PdO. In particular we compare with the data obtained by Monteiro et al.,[37] Martin et al.,[21] and Zhu et al.[16] These experiments cover a temperature range between 570 to 870 K and 3 orders of magnitude in total methane and oxygen pressures. As we study complete oxidation, desorption of intermediates is not included and the gas phase pressures are given by CH_4, O_2, and H_2O, whereas CO_2 desorption is assumed to be irreversible.

Kinetic Behavior. The comparison between the kinetic simulations and the experiments is shown in Table 3.

Table 3. Comparison of Measured and Simulated Reaction Orders and Apparent Activation Energies under Different Sets of Reaction Conditions (See Text)

		$E_{act,app}$	reaction orders		
	T (K)	(eV)	CH_4	O_2	H_2O
Monteiro et al.	570−630	1.30	0.7	0.2	−0.9
kinetic model		0.97	0.98	0.26	−0.67
Martin et al.	650−770	0.72	–	–	–
kinetic model		0.80	0.73	0.27	−0.27
Zhu et al.	780−870	0.31	0.6	0.0	0.0
kinetic model		0.27	0.89	0.06	−0.09

Depending on the reaction conditions, the calculated apparent activation energies vary from 0.27 to 0.97 eV. The largest difference in reaction orders is predicted for water (−0.67 to −0.09), whereas the reactions orders for oxygen and methane show smaller variations with respect to reaction conditions. The calculated kinetic properties compare favorably with the experimental data.

In the experiments by Monteiro et al.,[37] methane oxidation is investigated around 600 K with methane, oxygen and water pressures in the 10 mbar, 100 mbar, and 1 mbar range, respectively. The positive reaction order in methane is owing to the rate-limiting character of the dissociative adsorption of methane, i.e., this elementary step is the slowest within the entire pathway. To some extent, this is surprising, as the energy barrier for this reaction is only 0.29 eV, which is considerably lower than the energy barrier for the main subsequent reaction which involves a CH_3−H pair and adsorbed O (0.88 eV). However, in contrast to the surface reactions, the adsorption event possesses a considerable entropic barrier, which results in a high free energy barrier. Interestingly, also a second channel for dissociative methane adsorption contributes with ca. 20−30% to the total adsorption rate, namely the reaction with adsorbed OH producing adsorbed CH_3 and H_2O.

Although dissociative adsorption of methane is the reaction that mainly limits the total rate, the decomposition of the resulting CH_3−H pairs is not fast enough to completely prevent partial redesorption to gaseous CH_4. As the main reaction route for the CH_3−H is O-association, this effects yields a small positive order in oxygen pressure, which also is observed experimentally.

Another factor that limits the reaction rate, is the adsorption of water blocking the S_1 Pd sites, which are required for the adsorption of methane. This results in the negative reaction order in water and is the reason for an apparent activation energy that is much higher than the barrier for dissociative adsorption of methane. The water inhibition of methane adsorption on PdO(101) has previously been observed experimentally.[34]

Calculated coverages of selected adsorbates and turnover frequencies under conditions similar to the ones in ref 37 are presented in Figure 4. At low temperatures, the S_1 sites are covered predominately by water whereas S_2 sites have an appreciable coverage of hydrogen. The high coverage of adsorbed H_2O offers a molecular understanding of the experimentally observed water inhibition.[12] Methyl is predicted to be the most abundant carbonaceous species over the entire temperature range, except at temperatures below 550 K where CH_2 is accumulated on S_{2b} sites. The turnover frequency has an interesting temperature dependence. In the low temperature regime (500−630 K), the gradient corresponds to the previously discussed water inhibition conditions with an apparent activation energy of 0.92 eV. At high temperatures (900−1000 K), the gradient is decreased as methane

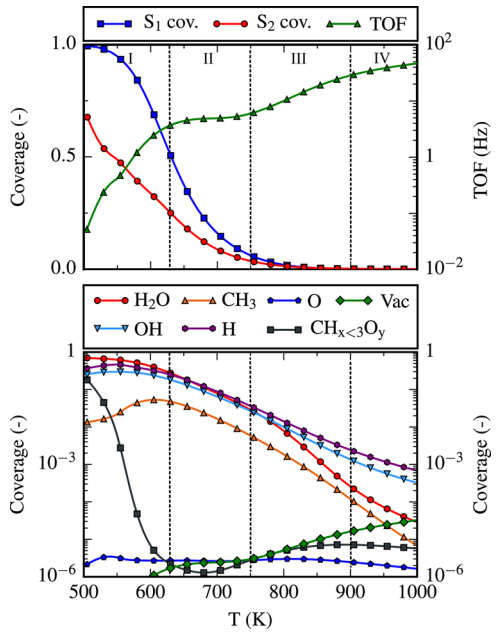

Figure 4. Calculated total site coverages and turnover frequencies (top) and coverages of selected relevant adsorbates (bottom) as a function of temperature. The gas phase pressures are typical of the experiments by Monteiro et al. (p_{CH_4} = 21 mbar, p_{O_2} = 213 mbar, p_{H_2O} = 1.3 mbar).

DOI: 10.1021/jacs.5b06069
J. Am. Chem. Soc. 2015, 137, 12035−12044

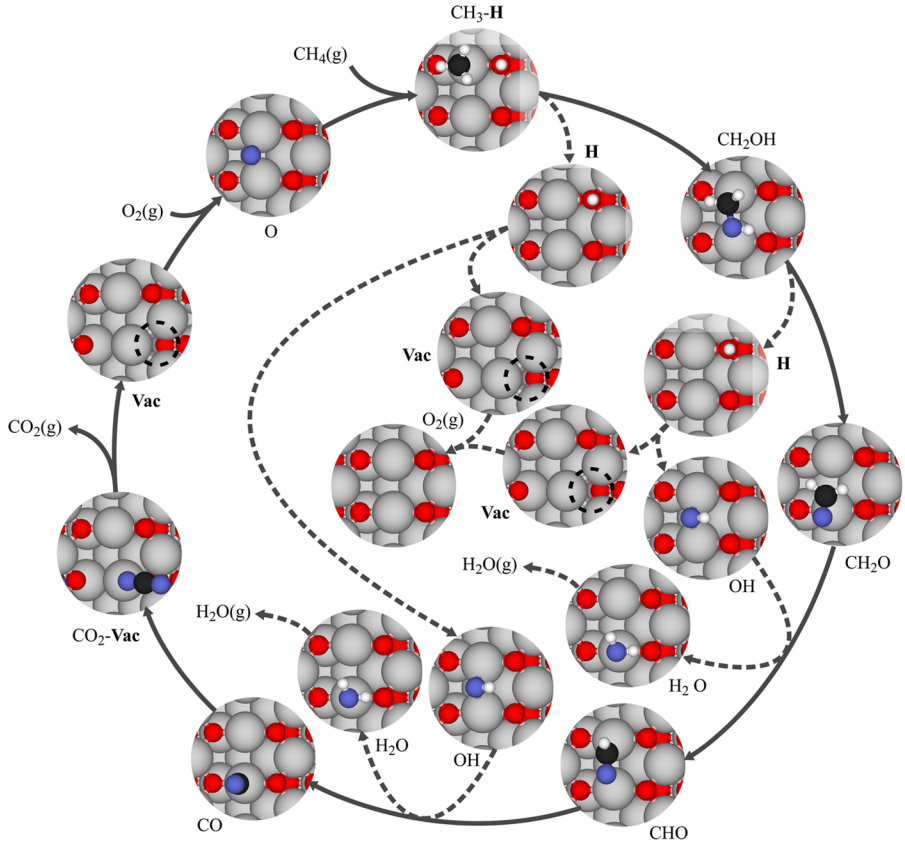

Figure 5. Main reaction pathway for the conversion of methane to carbon dioxide and water over the PdO(101) surface at the conditions of Monteiro et al.[37] Full arrows indicate the carbonaceous intermediates, whereas dashed arrows show the creation of other surface intermediates. Color code as in Figure 1 with adsorbed oxygen colored blue.

dissociation becomes the sole rate-determining step and the apparent activation energy is 0.38 eV.

Between 630 and 900 K (regions II and III), the kinetic behavior described by the model is more complex, as methyl (CH_3) decomposition together with methane dissociation are controlling the rate. In region II (630−750 K), the rate of methyl decomposition increases slower than the rate of methane desorption. This results in a rather weak temperature dependence of the TOF in this region, with an apparent activation energy of 0.12 eV. In region III (750−900 K), the methyl decomposition starts to take place via alternative pathways with higher activation energies (direct C−H dissociation) than for methane desorption. Since both methane adsorption and methyl decomposition become kinetically relevant, the apparent activation energy is higher than the barrier for methane adsorption, and takes a value of 0.64 eV.

In the experiments by Martin et al.,[21] the reaction was carried out over oxidized Pd(100) at temperatures between 650 and 770 K and total pressures close to 1 mbar range. Importantly, the formation of a thin PdO(101) film was confirmed by core-level spectroscopy. The apparent activation energy is in this case 0.8 eV. This is considerably lower than the value reported by Monteiro et al., but still higher than the calculated electronic energy barrier for dissociative adsorption of methane. The kinetic model shows that this is related to the relatively slow decomposition of CH_3, which leads to a redesorption of 20−40% of the CH_3−H groups to gaseous CH_4. This is reflected also in the calculated reaction order in methane beeing 0.73, which is significantly below unity. The slow CH_3 decomposition is furthermore connected to the presence of adsorbed H atoms and the formation of stable CH_3−H pairs. Hydrogen is in this case the most abundant surface species with ca. 0.1% coverage on S_2 oxygen sites. The presence of H on the surface has been observed experimentally by XPS measurements of the O 1*s* core-level.[21]

The work of Zhu et al.[16] addresses the oxidation at higher temperatures (780−870 K) and at partial pressures in methane, oxygen, and water pressures in the 0.2 mbar, 1 mbar, and 1 mbar range. Under these conditions, the low measured and calculated apparent activation energy (0.3 eV) shows that the dissociative adsorption of methane is the reaction that governs the rate of the total oxidation. This is one case where the improved accuracy of the HSE06 functional over the PBE functional is clearly visible. If instead the PBE value for the dissociative adsorption of methane would be used, an apparent activation energy of ca. 0.5 eV would be obtained (see reaction 1 in Table 1). Further information on the sensitivity of the predicted kinetic behavior on the exchange-correlation functional is available in the Supporting Information. Also under these conditions, about 20% of CH_3−H redesorbs before further reaction. As in the case of Martin et al.,[21] this leads to a below-unity reaction order in methane pressure. An increased pressure of methane yields a higher concentration of adsorbed H atoms which leads to a slight increase in the redesorption due to a higher fraction of CH_3 species that is present as CH_3−H pairs.

Reaction Mechanisms (Low Temperature). The main predicted pathway for oxidation of methane under the conditions used by Monteiro et al. is shown in Figure 5. Methane is dissociatively adsorbed with formation of a CH_3−H

DOI: 10.1021/jacs.5b06069
J. Am. Chem. Soc. 2015, 137, 12035−12044

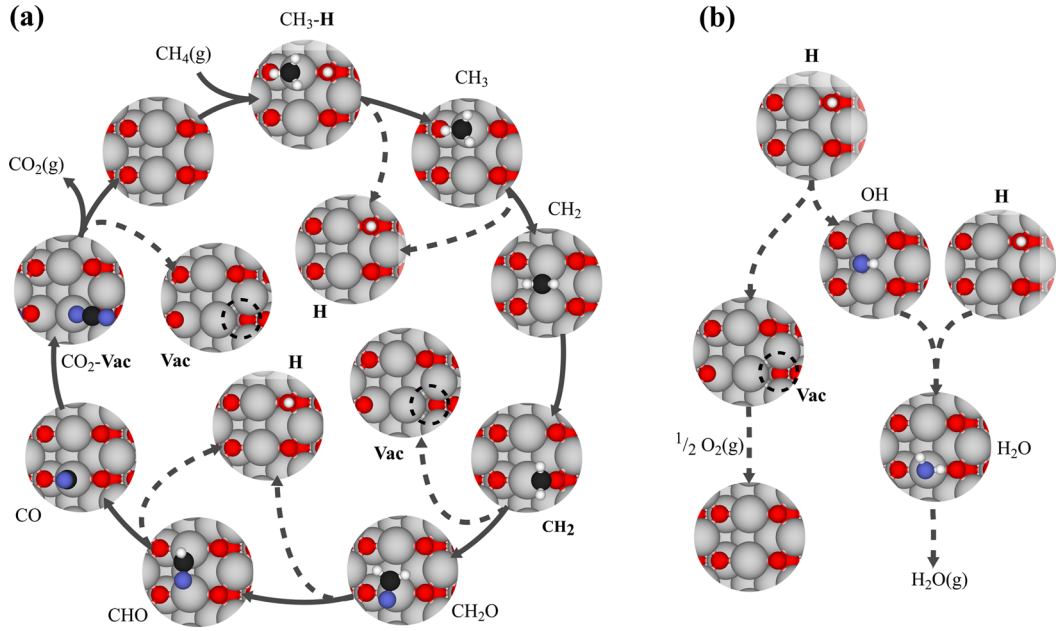

Figure 6. Main reaction pathway for the conversion of methane to carbon dioxide and water over the PdO(101) surface at the conditions of Martin et al.[21] and Zhu et al.[16] Full arrows indicate the carbonaceous intermediates, whereas dashed arrows show the creation of other surface intermediates. Color code as in Figure 1 with adsorbed oxygen colored blue.

pair. Considering first the carbonaceous intermediates, the methyl group is converted into hydroxymethylene (CH_2OH) by reaction with adsorbed oxygen. This species dissociates to formaldehyde (CH_2O) with hydrogen transfer to a lattice oxygen. Further dissociation via formyl (CHO) toward CO preferably occurs by reaction with adsorbed OH groups. Finally, CO_2 is formed by a reaction with lattice oxygen. The resulting oxygen vacancy is healed by adsorption and dissociation of O_2. This produces an adsorbed O atom, which can either close the catalytic cycle and react with a CH_3−H pair or heal another oxygen vacancy. In the mechanism, water is formed from H atoms adsorbed on the S_{2a} oxygen sites. The OH group detaches from the lattice and occupies a S_{1b} palladium site in a process that involves the creation of an oxygen vacancy. Water is subsequently formed by a reaction between OH and CH_2O or CHO. The oxygen vacancy is healed by adsorption of molecular oxygen.

We find that the incorporation of the first oxygen atom into the carbon containing moiety occurs at an early stage and proceeds mainly via a Langmuir−Hinshelwood mechanism. Because of the exothermicity of the C−O bond formation process, this path is preferred with respect to further dissociation into CH_2, CH, and elemental carbon intermediates. Early C−O bond formation has also been suggested in a recent theoretical study addressing the mechanism for CH_4 oxidation over the PdO(100) surface.[26] The incorporation of the second oxygen atom, forming carbon dioxide, takes place in a Mars−van Krevelen step. This finding is in agreement with kinetic isotope studies[36,65,66] carried out in the same temperature regime, which suggest that oxygen in the final product mainly originates from oxygen in the bulk PdO and partly from oxygen in O_2 gas. In the mechanism, adsorbed O species are produced mainly by adsorption and subsequent dissociation of O_2 on oxygen vacancies. Dissociation of O_2 adsorbed over Pd surface sites is both endothermic and highly activated (see reaction 8 in Table 2).

Reaction Mechanisms (High Temperature). At higher temperatures, as in the experiments by Martin et al.[21] and Zhu et al.,[16] the kinetic model reveals a slightly different mechanism, as shown in Figure 6. Because of the higher temperatures and lower O_2 pressures, the concentration of adsorbed O and OH are low and decomposition of CH_x species preferentially occurs by reaction with S_{2a} oxygen sites. In this way, methyl dissociates into methylene and a hydrogen on an S_{2a} site. Formaldehyde is subsequently formed by reaction of the methylene group with yet another surface oxygen. Two sequential dissociation steps produce adsorbed CO. As in the low temperature case, CO reacts with oxygen from the lattice, producing CO_2. Water formation occurs by a combination of adsorbed H atoms and OH groups as shown in Figure 6(b). This step results in an oxygen vacancy that is healed by gas phase oxygen.

Compared to the low temperate mechanism, there is at elevated temperatures a higher participation of the lattice oxygen atoms, both for dissociation reactions and oxygen addition reactions through Mars−van Krevelen mechanisms. However, it should be noted that reactions may occur in the gas phase. Adsorbed methyl and formaldehyde, for example, may desorb from the surface before further decomposition if the temperature is sufficiently high. The present kinetic model assumes that the gas phase reactions are slow, so that the entire conversion to CO_2 proceeds on the surface.

■ CONCLUSIONS

A detailed kinetic model has been constructed that is able to describe the oxidation kinetics and reaction intermediates for the total oxidation of methane over the PdO(101) surface from first principles. The model reproduces measured data in wide temperature and pressure ranges. The good agreement with various experimental findings offers, for the first time, a molecular understanding of the kinetic behavior of methane oxidation over PdO catalysts. In particular, the atomic level understanding resolves previous puzzles in the kinetic behavior,

DOI: 10.1021/jacs.5b06069
J. Am. Chem. Soc. 2015, 137, 12035−12044

such as a sizable variation in measured apparent activation energies and reaction orders in methane below unity. The low temperature reaction pathway involves early insertion of oxygen in carbonaceous species and C−H scission by reaction with OH groups. The OH-coverage at high temperatures is low, favoring C−H bond breaking through reaction with lattice oxygen atoms. In both temperature regimes, oxidation steps take place through Mars−van Krevelen mechanisms, which is the dominating route at high temperatures. The reaction is found to be poisoned by molecular water adsorbed on under-coordinated Pd-sites at low temperatures. This finding offers molecular understanding of the measured water inhibition. This information provides new starting points for the computational design of materials with improved catalytic activity. One example is the finding that the dissociative adsorption of methane is the sole rate-determining step only at high temperatures. This implies that efforts to enhance the low temperature activity of palladium-based catalysts should be directed to facilitate methyl decomposition and reduce effects of water inhibition. Although the presented results have been obtained for unsupported PdO(101), their validity for supported catalysts can be inferred from the fact that the reaction orders and apparent activation energies reported for Pd supported on Al_2O_3 and ZrO_2 are qualitatively similar to those measured for unsupported PdO.[67]

The satisfying agreement between the FP-MKM results and experiments was possible through an accurate theoretical description of the electronic structure by use of a hybrid functional and kinetic modeling beyond the mean-field approximation. Moreover, the findings illustrate that calculated activation energies do not always directly correspond to measured apparent activation energies. Instead, kinetic simulations with all relevant reactions are required for accurate comparisons. The demonstrated success of this methodology for such a complex reaction as complete methane oxidation opens up the possibility to use similar approaches for understanding and design of catalysts.

■ ASSOCIATED CONTENT

Supporting Information

The Supporting Information is available free of charge on the ACS Publications website at DOI: 10.1021/jacs.5b06069.

Additional information on the origin of the electronic pairing, a detailed account of the kinetic model, and an analysis of the sensitivity to the exchange-correlation functional and the inclusion of the pairing interactions. (PDF)

All investigated structures. (ZIP)

■ AUTHOR INFORMATION

Corresponding Authors

*bossche@chalmers.se

*ghj@chalmers.se

Notes

The authors declare no competing financial interest.

■ ACKNOWLEDGMENTS

Financial support is acknowledged from the Swedish Research Council, Chalmers Areas of Advance Nano and Transport, NordForsk, and COST action CM1104. The calculations were performed at C3SE (Göteborg) and PDC (Stockholm) via a SNIC grant. The Competence Centre for Catalysis (KCK) is hosted by Chalmers University of Technology and is financially supported by the Swedish Energy Agency and the member companies: AB Volvo, ECAPS AB, Haldor Topsøe A/S, Scania CV AB, Volvo Car Corporation AB, and Wärtsila Finland Oy.

■ REFERENCES

(1) Somorjai, G. A. *Chem. Rev.* **1996**, *96*, 1223−1236.

(2) Ogletree, D.; Bluhm, H.; Lebedev, G.; Fadley, C.; Hussain, Z.; Salmeron, M. *Rev. Sci. Instrum.* **2002**, *73*, 3872.

(3) Öström, H.; et al. *Science* **2015**, *347*, 978−982.

(4) López, N.; Almora-Barrios, N.; Carchini, G.; Błoński, P.; Bellarosa, L.; García-Muelas, R.; Novell-Leruth, G.; García-Mota, M. *Catal. Sci. Technol.* **2012**, *2*, 2405−2417.

(5) Sabbe, M. K.; Reyniers, M.-F.; Reuter, K. *Catal. Sci. Technol.* **2012**, *2*, 2010.

(6) Honkala, K.; Hellman, A.; Remediakis, I. N.; Logadottir, A.; Carlsson, A.; Dahl, S.; Christensen, C. H.; Nørskov, J. K. *Science* **2005**, *307*, 555−558.

(7) Reuter, K.; Scheffler, M. *Phys. Rev. B: Condens. Matter Mater. Phys.* **2006**, *73*, 045433.

(8) Linic, S.; Barteau, M. A. *J. Am. Chem. Soc.* **2003**, *125*, 4034−4035.

(9) Greeley, J.; Mavrikakis, M. *J. Am. Chem. Soc.* **2004**, *126*, 3910−3919.

(10) Gokhale, A. A.; Dumesic, J. A.; Mavrikakis, M. *J. Am. Chem. Soc.* **2008**, *130*, 1402−1414.

(11) Rozanska, X.; Fortrie, R.; Sauer, J. *J. Am. Chem. Soc.* **2014**, *136*, 7751−7761.

(12) Ciuparu, D.; Lyubovsky, M. R.; Altman, E.; Pfefferle, L. D.; Datye, A. *Catal. Rev.: Sci. Eng.* **2002**, *44*, 593−649.

(13) Horn, R.; Schlögl, R. *Catal. Lett.* **2015**, *145*, 23.

(14) Burch, R.; Urbano, F.; Loader, P. *Appl. Catal., A* **1995**, *123*, 173.

(15) Burch, R.; Loader, P.; Urbano, F. *Catal. Today* **1996**, *27*, 243.

(16) Zhu, G.; Han, J.; Zemlyanov, D. Y.; Ribeiro, F. H. *J. Phys. Chem. B* **2005**, *109*, 2331−2337.

(17) Gabasch, H.; Hayek, K.; Klötzer, B.; Unterberger, W.; Kleimenov, E.; Teschner, D.; Zafeiratos, S.; Hävecker, M.; Knop-Gericke, A.; Schlögl, R.; Aszalos-Kiss, B.; Zemlyanov, D. *J. Phys. Chem. C* **2007**, *111*, 7957−7962.

(18) Matam, S. K.; Aguirre, M. H.; Weidenkaff, A.; Ferri, D. *J. Phys. Chem. C* **2010**, *114*, 9439−9443.

(19) Hellman, A.; Resta, A.; Martin, N. M.; Gustafson, J.; Trinchero, A.; Carlsson, P.-A.; Balmes, O.; Felici, R.; van Rijn, R.; Frenken, J. W. M.; Andersen, J. N.; Lundgren, E.; Grönbeck, H. *J. Phys. Chem. Lett.* **2012**, *3*, 678−682.

(20) Chin, Y.-H.; Buda, C.; Neurock, M.; Iglesia, E. *J. Am. Chem. Soc.* **2011**, *133*, 15958−15978.

(21) Martin, N. M.; Van den Bossche, M.; Hellman, A.; Grönbeck, H.; Hakanoglu, C.; Gustafson, J.; Blomberg, S.; Johansson, N.; Liu, Z.; Axnanda, S.; Weaver, J. F.; Lundgren, E. *ACS Catal.* **2014**, *4*, 3330−3334.

(22) Weaver, J. F.; Hakanoglu, C.; Hawkins, J. M.; Asthagiri, A. *J. Chem. Phys.* **2010**, *132*, 024709.

(23) Antony, A.; Asthagiri, A.; Weaver, J. F. *J. Chem. Phys.* **2013**, *139*, 104702.

(24) Rogal, J.; Reuter, K.; Scheffler, M. *Phys. Rev. B: Condens. Matter Mater. Phys.* **2004**, *69*, 075421.

(25) Blanco-Rey, M.; Jenkins, S. J. *J. Chem. Phys.* **2009**, *130*, 014705.

(26) Dianat, A.; Seriani, N.; Ciacchi, L. C.; Bobeth, M.; Cuniberti, G. *Chem. Phys.* **2014**, *443*, 53−60.

(27) Martin, N. M.; Van den Bossche, M.; Grönbeck, H.; Hakanoglu, C.; Zhang, F.; Li, T.; Gustafson, J.; Weaver, J. F.; Lundgren, E. *J. Phys. Chem. C* **2014**, *118*, 1118−1128.

(28) Hirvi, J. T.; Kinnunen, T.-J. J.; Suvanto, M.; Pakkanen, T. A.; Nørskov, J. K. *J. Chem. Phys.* **2010**, *133*, 084704.

(29) Martin, N. M.; Van den Bossche, M.; Grönbeck, H.; Hakanoglu, C.; Gustafson, J.; Blomberg, S.; Arman, M. A.; Antony, A.; Rai, R.; Asthagiri, A.; Weaver, J. F.; Lundgren, E. *J. Phys. Chem. C* **2013**, *117*, 13510−13519.

DOI: 10.1021/jacs.5b06069
J. Am. Chem. Soc. 2015, 137, 12035−12044

(30) Hakanoglu, C.; Hawkins, J. M.; Asthagiri, A.; Weaver, J. F. *J. Phys. Chem. C* **2010**, *114*, 11485−11497.
(31) Hinojosa, J.; Jose, A.; Kan, H. H.; Weaver, J. F. *J. Phys. Chem. C* **2008**, *112*, 8324−8331.
(32) Kan, H. H.; Colmyer, R. J.; Asthagiri, A.; Weaver, J. F. *J. Phys. Chem. C* **2009**, *113*, 1495−1506.
(33) Hinojosa, J. A.; Antony, A.; Hakanoglu, C.; Asthagiri, A.; Weaver, J. F. *J. Phys. Chem. C* **2012**, *116*, 3007−3016.
(34) Zhang, F.; Hakanoglu, C.; Hinojosa, J. A., Jr.; Weaver, J. F. *Surf. Sci.* **2013**, *617*, 249−255.
(35) Weaver, J. F.; Hinojosa, J. A., Jr.; Hakanoglu, C.; Antony, A.; Hawkins, J. M.; Asthagiri, A. *Catal. Today* **2011**, *160*, 213−227.
(36) Au-Yeung, J.; Chen, K.; Bell, A. T.; Iglesia, E. *J. Catal.* **1999**, *188*, 132−139.
(37) Monteiro, R. S.; Zemlyanov, D.; Storey, J. M.; Ribeiro, F. H. *J. Catal.* **2001**, *199*, 291−301.
(38) Hickman, D. A.; Schmidt, L. D. *AIChE J.* **1993**, *39*, 1164−1177.
(39) Trinchero, A.; Hellman, A.; Grönbeck, H. *Surf. Sci.* **2013**, *616*, 206−213.
(40) Kresse, G.; Furthmüller, J. *Comput. Mater. Sci.* **1996**, *6*, 15−50.
(41) Kresse, G.; Furthmüller, J. *Phys. Rev. B: Condens. Matter Mater. Phys.* **1996**, *54*, 11169−11186.
(42) Kresse, G.; Hafner, J. *Phys. Rev. B: Condens. Matter Mater. Phys.* **1994**, *49*, 14251−14269.
(43) Momma, K.; Izumi, F. *J. Appl. Crystallogr.* **2011**, *44*, 1272−1276.
(44) The procedure to contrain the bottom layers was tested by considering full relaxation for adsorbed (CH_3+H) and H_2O. In both cases, the differences were calculated to be below 7 meV.
(45) Henkelman, G.; Jonsson, H. *J. Chem. Phys.* **2000**, *113*, 9978−9985.
(46) Henkelman, G.; Uberuaga, B.; Jonsson, H. *J. Chem. Phys.* **2000**, *113*, 9901−9904.
(47) Henkelman, G.; Jónsson, H. *J. Chem. Phys.* **1999**, *111*, 7010−7022.
(48) Okamoto, H.; Asô, T. *Jpn. J. Appl. Phys.* **1967**, *6*, 779−779.
(49) Nilsson, P. O. *J. Phys. C: Solid State Phys.* **1979**, *12*, 1423.
(50) Seriani, N.; Harl, J.; Mittendorfer, F.; Kresse, G. *J. Chem. Phys.* **2009**, *131*, 054701.
(51) Van den Bossche, M.; Martin, N. M.; Gustafson, J.; Hakanoglu, C.; Weaver, J. F.; Lundgren, E.; Grönbeck, H. *J. Chem. Phys.* **2014**, *141*, 034706.
(52) Heyd, J.; Scuseria, G. E.; Ernzerhof, M. *J. Chem. Phys.* **2003**, *118*, 8207−8215.
(53) Heyd, J.; Scuseria, G. E.; Ernzerhof, M. *J. Chem. Phys.* **2006**, *124*, 219906.
(54) Heyd, J.; Scuseria, G. E. *J. Chem. Phys.* **2004**, *121*, 1187−1192.
(55) Grimme, S.; Antony, J.; Ehrlich, S.; Krieg, H. *J. Chem. Phys.* **2010**, *132*, 154104.
(56) Perdew, J. P.; Burke, K.; Ernzerhof, M. *Phys. Rev. Lett.* **1996**, *77*, 3865−3868.
(57) Eyring, H. *J. Chem. Phys.* **1935**, *3*, 107−115.
(58) Evans, M. G.; Polanyi, M. *Trans. Faraday Soc.* **1935**, *31*, 875−894.
(59) Abbott, H. L.; Harrison, I. *J. Catal.* **2008**, *254*, 27−38.
(60) Hindmarsh, A. *IMACS Trans. Sci. Comput.* **1983**, *1*, 55−64.
(61) As methane is weakly bonded to the surface, the rate coefficient for desorption from the adsorbed molecular state is much larger than for dissociation. At such conditions it is adequate to describe methane dissociation as dissociative adsorption from the gas-phase. The activation energy for methane dissociation over S_1 from the molecular adsorbed state is calculated to be 0.56 (0.67) eV within HSE06 (PBE).
(62) Weaver, J. F. *Chem. Rev.* **2013**, *113*, 4164−4215.
(63) Broqvist, P.; Grönbeck, H.; Fridell, E.; Panas, I. *J. Phys. Chem. B* **2004**, *108*, 3523.
(64) Schneider, W. F. *J. Phys. Chem. B* **2004**, *108*, 273−282.
(65) Müller, C. A.; Maciejewski, M.; Koeppel, R. A.; Tschan, R.; Baiker, A. *J. Phys. Chem.* **1996**, *100*, 20006−20014.
(66) Ciuparu, D.; Altman, E.; Pfefferle, L. *J. Catal.* **2001**, *203*, 64−74.
(67) Zhu, G.; Han, J.; Zemlyanov, D. Y.; Ribeiro, F. H. *J. Am. Chem. Soc.* **2004**, *126*, 9896−9897.

DOI: 10.1021/jacs.5b06069
J. Am. Chem. Soc. 2015, 137, 12035−12044